

Article

A Low-Inertia and High-Stiffness Cable-Driven Biped Robot: Design, Modeling, and Control

Jun Tang ^{1,2}, Haiming Mou ^{1,2} , Yunfeng Hou ^{2,*} , Yudi Zhu ², Jian Liu ²  and Jianwei Zhang ³

¹ School of Optical-Electrical and Computer Engineering, University of Shanghai for Science and Technology, Shanghai 200093, China; 211240187@st.usst.edu.cn (J.T.); 201440059@st.usst.edu.cn (H.M.)

² Institute of Machine Intelligence, University of Shanghai for Science and Technology, Shanghai 200093, China; 221240082@st.usst.edu.cn (Y.Z.); liujian92@usst.edu.cn (J.L.)

³ Department of Informatics, University of Hamburg, 20146 Hamburg, Germany

* Correspondence: yunfenghou@usst.edu.cn; Tel.: +86-1521-672-1916

Abstract: In this paper, a biped robot system for dynamic walking is presented. It has two 2-degree-of-freedom (DOF) lightweight legs and a 6-DOF hip. All the joint pulleys of the legs are driven by motors that are placed at the hip using steel cables. Since all the heavy motors are mounted at the hip, the biped robot has remarkably low-mass legs beyond the hip, which guarantees low inertia during walking at high speeds. Utilizing cable-amplification mechanisms, high stiffness and strength are achieved, resulting in better control performance compared to conventional direct-driven methods. Techniques are developed to estimate joint-angle errors caused by the elastic deformation of the cables. To achieve smooth control, we introduce the concept of a virtual leg, which is an imaginary leg connecting the hip joint and the ankle joint. A robust control approach based on the “virtual leg” is presented, which considers the variances of the virtual leg length during walking. Experiments are conducted to validate the effectiveness of the mechanical design and the proposed control approach.

Keywords: biped robot; cable driven; low inertia; high stiffness; joint-angle error; virtual leg

MSC: 70E60



Citation: Tang, J.; Mou, H.; Hou, Y.; Zhu, Y.; Liu, J.; Zhang, J. A Low-Inertia and High-Stiffness Cable-Driven Biped Robot: Design, Modeling, and Control. *Mathematics* **2024**, *12*, 559. <https://doi.org/10.3390/math12040559>

Academic Editor: Asier Ibeas

Received: 16 January 2024

Revised: 4 February 2024

Accepted: 8 February 2024

Published: 13 February 2024



Copyright: © 2024 by the authors. Licensee MDPI, Basel, Switzerland. This article is an open access article distributed under the terms and conditions of the Creative Commons Attribution (CC BY) license (<https://creativecommons.org/licenses/by/4.0/>).

1. Introduction

One of the most common approaches for generating walking trajectories for humanoid robots is to exploit the entire dynamics of the robot. However, it is time-consuming to solve the high-dimensional nonlinear optimization problem. Thus, to generate walking patterns on the fly, a simplified linear model that captures the kinetic characteristics of the robot is necessary. In this regard, the linear inverted pendulum model (LIPM) has been widely used to design controllers for complex biped robots.

By augmenting with controllable inputs, Ernesto et al. [1] proposed the non-homogeneous LIPM (NH-LIPM), which allows for parameter control compared to the traditional LIPM. Through regression, it was shown in [1] that the parameters of the NH-LIPM can be extracted and tuned using the recursive least-square algorithm. By combining an Ant Lion Optimization (ALO)-tuned LIPM with a flywheel, the authors of [2] developed a robust walking gait generation method. Using the LIPM and the norm-based stability criterion, Hae Yeon et al. [3] proposed two approaches for controlling biped robot walking, discussing the dynamic relationship between the Center of Mass (COM) and the Zero-Moment Point (ZMP). A novel bipedal stepping control method was proposed in [4] by analyzing the phase space of the COM using the LIPM. Additionally, the authors of [4] achieved stable alternate stepping without pre-defined trajectories. The results were validated through computer simulations in [4]. A flexible LIPM was introduced in [5], where the constraints encountered when accommodating joint flexibility in robots were overcome. A damped

spring and an additional COM were empirically demonstrated to surpass the constraints caused by the LIPM to attain stable walking motions [5].

The LIPM considers the legs of the robot as a light rod, which has infinitesimally small mass and infinite stiffness. However, in reality, the legs of a robot do have mass, and their angular momentum plays a role in the overall dynamics of the system. In practical scenarios, especially for robots where the motors are mounted at the joints, the mass and angular momentum of the legs cannot be ignored when analyzing the motion and stability of a robot. Generally, approaches for overcoming discrepancies between the mathematical model used to represent the robot's dynamics and its actual behavior can be categorized into two categories. For the first category, techniques, for example, reinforcement learning algorithms [6–8] and robust estimation and control algorithms [9–13], are developed to offset and overcome the mismatch between the real robot dynamics and the dynamics of the simplified model. For the second category, lightweight and low-inertia robots are designed to reduce modeling errors and enhance the stability of a robot [14–19].

In this paper, we focus on designing and controlling a low-inertia and high-stiffness cable-driven biped leg robot. Using a cable-driven leg, a novel heuristic landing planner was proposed in [20]. To overcome the external disturbances and uncertainties, the landing locations are adjusted in real time with the feedback of the momentum during the flight phase. The authors of [21] designed a 3-DOF-leg robot that is driven by four cables. To achieve the desired motion, techniques were proposed to identify the cable configurations of the robot. Evandro et al. proposed a novel cable-driven ankle-foot robot with two controllable DOFs in both dorsiflexion-plantar flexion and inversion-eversion [22]. This robot has several human-like characteristics, such as power, range of motion, and weight, which indicate the design's feasibility. Meanwhile, to address gait impairments for individuals with chronic hemiparesis post-stroke, Rand Hidayah et al. introduced the cable-driven active leg exoskeleton (C-ALEX) [23], which allows unrestricted movement and continuous force assistance using the gait cycle. Experimental results showed that the C-ALEX can provide accurate forces and torques as expected. The authors of [24] introduced a new cable-constrained parallel-legged walking mechanism, which is lightweight and cost-effective and has three translational DOFs. Experimental validation showed that it can effectively track a planar walking trajectory by using a real-time PCI controller.

In this paper, by integrating planetary gears and cable-driven deceleration techniques, we propose a cable-driven biped robot, which has two 2-DOF lightweight legs and a 6-DOF hip. To guarantee that the robot has low inertia during walking, all the heavy motors are mounted at the hip, which leads to a relatively low-mass leg. Specifically, the hip joints are directly driven by the motors, but the knee joints and the ankle joints are driven by motors mounted at the hip over cables. This lightweight leg design leads to low inertia and enhances the response speed of the robotic system. That is, the low inertia requires less energy to achieve the same acceleration and speed during walking. Meanwhile, the lightweight leg is more sensitive to external forces or control inputs, enabling more precise control and adjustment.

The backlash, or equivalently, the clearance between gears in a drive train, can affect the accuracy of a robot's movements. By reducing the backlash through a properly adjusted reduction ratio, the robot can achieve more precise and repeatable motions, leading to higher control performance. In this paper, since the joint pulley is connected to the motor via cables, the speed is reduced when the motor motion is transmitted to the joint pulley. As a result, the effect of the motor backlash on the joints can be reduced. In addition, since the cable itself has elasticity, it can absorb the force when the joint experiences a significant impact, thereby reducing the effect of the impact on the gears of the motor. To compensate for errors caused by the elastic deformation of the steel cables, a joint-angle error estimation approach is introduced based on Hooke's law and the motor characteristics. Since joints are tightly coupled, it is difficult to realize robust dynamic walking, especially since indeterministic control errors always exist. To address this issue, we introduce the notion of the "virtual leg", which connects the hip joint and the ankle joint. A robust control

approach based on the “virtual leg” is presented, which minimizes the variance of the virtual leg length so that the movements of all the joints can be well coordinated during walking. Experimental results show the effectiveness of the proposed control approach.

The rest of this paper is organized as follows. Section 2 introduces the mechanical design. Section 3 estimates the errors caused by the elastic deformation of the steel cables. Section 4 shows how dynamic walking is realized. We conduct experiments in Section 5. Section 6 presents the conclusions.

2. Mechanical Design

In this paper, we name our biped robot “M03”. Figure 1 illustrates the kinematic structure of M03, which comprises a torso, a hip, and two legs. The M03 biped robot has 10 joints, with each leg comprising 2 joints (1 for knee pitch and 1 for ankle pitch), and the hip comprising 6 joints.

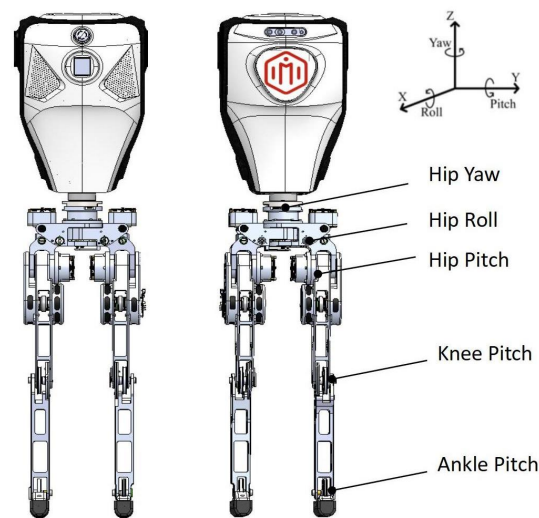


Figure 1. The mechanical structure of the biped robot.

2.1. Hip Design

Figure 2 displays our compact mechanical design of the robot’s hip, which integrates six motors (two for hip yaw, two for hip roll, and two for hip pitch) in total. In contrast to traditional approaches, the hip of M03 achieves yaw rotation functions for the torso, left hip, and right hip using only two motors. To be more specific, as shown in Figure 2, the first hip yaw motor connects the left hip to the torso, whereas the second hip yaw motor connects the left hip to the right hip. This design allows for independent and coordinated rotations of the torso and hips, reducing the need for additional motors and optimizing both weight and cost.

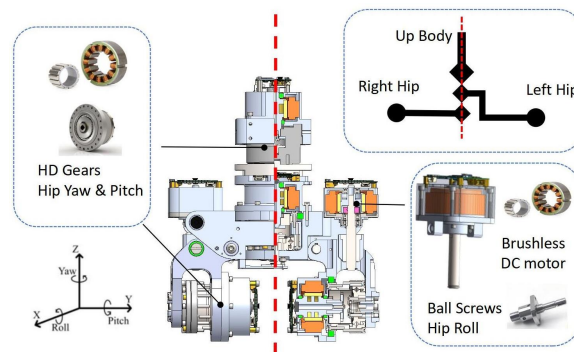


Figure 2. The mechanical structure of the hip.

2.2. Leg Design

As depicted in Figure 3, each leg consists of three parts: the upper legs, lower legs, and feet. Both the upper legs and lower legs have a length of 250 mm. To satisfy the lightweight and strength requirements, the upper and lower legs are made of 7075 aluminum alloy. Each leg exhibits 2 DOFs, corresponding to the knee joint and the ankle joint. Thus, there are four AK80-9 motors for the two legs, with each motor responsible for controlling a joint. These four AK80-9 motors are mounted on the sides of the upper legs (170 mm away from the knee joints) and are used to drive the motions of the knee and ankle joints. Unlike the hip joints, the motor motions are transmitted to the knee and ankle joints using TYPE-G steel cables with a diameter of 1.5 mm and a tensile strength of 260 KN. As shown in Figure 3, both the knee flexion cables and the ankle flexion cables come from the AK80-9 motors. The knee flexion cables wind around the knee pulley only, whereas the ankle flexion cables wind around the pulleys at the knee and the ankle. Because of the winding of the cables, the backlash of the motor gears decreases to one-third of its original value. By adjusting the reduction ratio, the backlash of the motor gears can be further reduced, resulting in high control performance. Additionally, this cable-driven framework raises the motors' positions, which effectively reduces the rotational inertia of the legs. The mass of each leg beyond the hip is only 1.980 kg, including 0.800 kg for the two AK80-9 motors, 0.340 kg for the upper legs, 0.211 kg for the lower legs, 0.245 kg for the feet, and 0.384 kg for the remaining mechanical parts, such as steel cables and screws. Table 1 presents the selected specifications of the robot.

Table 1. Specifications of the robot.

Item	Specifications
Peak torque	Hip yaw: 83 N·m Hip roll: 5000 N·m Hip pitch: 83 N·m Knee pitch: 54 N·m Ankle pitch: 36 N·m
Rang of motion	Hip yaw: −90 deg~90 deg Hip roll: −15 deg~20 deg Hip pitch: −60 deg~90 deg Knee pitch: −120 deg~5 deg Ankle pitch: −60 deg~60 deg
Speed	Hip yaw: 67 rpm Hip roll: 30 rpm Hip pitch: 67 rpm Knee pitch: 85 rpm Ankle pitch: 127 rpm
Way of actuation	Hip yaw: Servo Hip roll: Linkage Hip pitch: Serve Knee pitch: Tendon Ankle pitch: Tendon

Remark 1. Although reducing the backlash can improve control performance, increasing the gear reduction ratio may also increase the wear and tear on the gears and other mechanical components. Additionally, increasing the gear reduction ratio can increase the torque required to move the robot, which may require a more powerful motor.

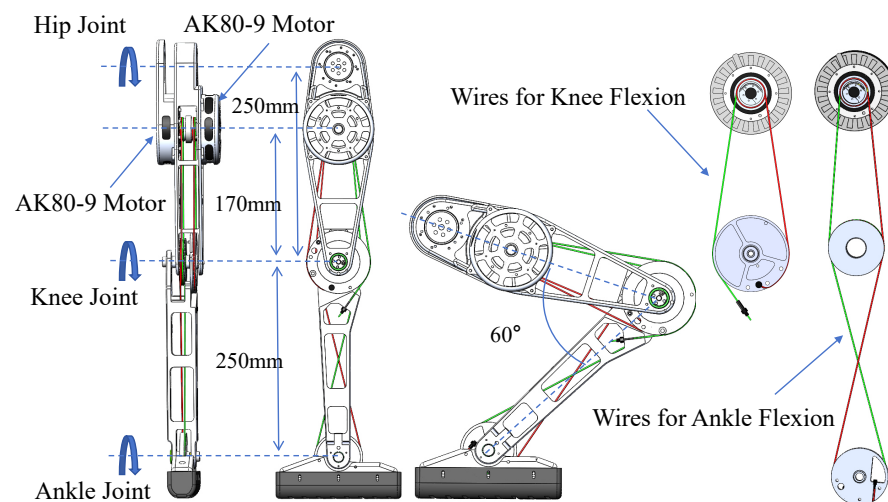


Figure 3. The mechanical structure of the legs.

3. Joint-Error Estimation

To guide the robot to the desired position, the forward kinematic equation is typically used to convert the joint angles into the end-effector pose. The inverse kinematic equation can then be used to convert the desired end-effector pose into the required joint angles. However, in practical applications, the motor driver requires motor angles or velocities as input signals. Therefore, an accurate mapping from the joint space to the motor space is necessary to convert the desired joint angles or velocities into the required motor angles or velocities. Next, we show how to estimate the joint errors caused by the motor execution error and the elastic deformation of the cables.

As shown in Figure 4, the translation movements of a steel cable are realized through the motor’s rotation. If there are no motor execution errors and no extension and slack in the cables, the joint motor and its driven pulley should have the same rotation distance. However, in practice, there always exists a motor execution error, i.e., the difference between the target position and the actual position of the motor. In addition, the steel cable undergoes slight elastic deformation, leading to a difference between the actual and desired positions of the knee-joint pulley. To enable precise control of the robot joints, joint position error estimation and compensation are necessary.

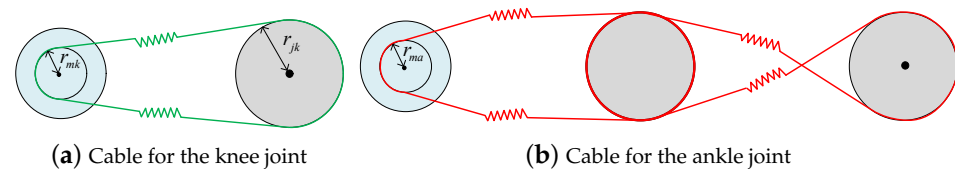


Figure 4. Routes of the cables.

First, we introduce some notations. We define m_{at} and m_{kt} as the target ankle motor position and target knee motor position, respectively. The current ankle motor position and current knee motor position are represented as m_{ac} and m_{kc} , respectively. In addition, we denote j_{at} and j_{kt} as the target ankle-joint position and target knee-joint position, respectively. We also denote j_{ac} and j_{kc} as the current ankle motor position and current knee motor position, respectively. The gear reduction ratios for the knee motor and the ankle motor are both 3:1 in this paper. Thus, the knee-joint position error and the ankle-joint position error caused by the elastic deformation of the steel cables are given as

$$e_{k,1} = 1/3m_{kc} - j_{kc}$$

$$e_{a,1} = 1/3m_{ac} - j_{ac}$$

In addition, let us define the knee-joint and ankle-joint errors caused by motor executions as

$$\begin{aligned} e_{k,2} &= 1/3(m_{kt} - m_{kc}) \\ e_{a,2} &= 1/3(m_{at} - m_{ac}) \end{aligned}$$

Overall, the knee-joint and ankle-joint position errors can, respectively, be expressed as:

$$\begin{aligned} e_k &= j_{kt} - j_{kc} = 1/3m_{kt} - j_{kc} = e_{k,1} + e_{k,2} \\ e_a &= j_{at} - j_{ac} = 1/3m_{at} - j_{ac} = e_{a,1} + e_{a,2} \end{aligned}$$

That is, the joint position error consists of two parts: the motor execution error and the elastic deformation error. The knee and ankle motor execution errors, i.e., $e_{k,2}$ and $e_{a,2}$, can be directly obtained using the absolute pulse coder mounted on the motors, and the elastic deformation errors for the knee joint and the ankle joint, i.e., $e_{k,1}$ and $e_{a,1}$, can be measured using Hooke’s law. To be more specific, we have

$$\begin{aligned} e_{k,1} &= F_k / K = \tau_{ma} / Kr_{ma} \\ e_{a,1} &= F_a / K = \tau_{mk} / Kr_{mk} \end{aligned}$$

where F_k and F_a are the forces exerted on the steel cables for the knee joint and ankle joint, respectively; τ_{mk} and τ_{ma} are the output torques of the knee-joint motor and the ankle-joint motor, respectively; r_{mk} and r_{ma} are the radii of the knee-motor pulley and ankle-motor pulley, respectively; and K is the elastic coefficient of the steel cables.

To control the ankle- and knee-joint angles to their target values, two PD controllers for the ankle-joint motor and the knee-joint motor can be easily obtained as follows:

$$\tau_{ja} = K_a(j_{at} - j_{ac}) + D_a(\dot{j}_{ac}) = K_a(e_{a1} + e_{a2}) = K_a(\tau_{ma} / Kr_{ma} + \frac{1}{3}(m_{at} - m_{ac})) + D_a(\frac{1}{3}\dot{m}_{ac}) \tag{1}$$

and

$$\tau_{jk} = K_k(j_{kt} - j_{kc}) + D_k(\dot{j}_{ac}) = K_{pk}(e_{k1} + e_{k2}) = K_k(\tau_{mk} / Kr_{mk} + \frac{1}{3}(m_{kt} - m_{kc})) + D_k(\frac{1}{3}\dot{m}_{ac}) \tag{2}$$

where K_a , D_a , K_k , and D_k are the PD parameters of the ankle-joint controller and the knee-joint controller. We note that instead of using (1) and (2), in the next section, we introduce the concept of the “virtual leg” and consider the variance of the virtual leg length when controlling the joint angles to their target values.

4. Control Strategy

4.1. Foot Landing Strategy

To determine the landing point of the robot at each step, we consider the LIPM for our simplified model. That is, the motion of the COM on a plane is constrained by the LIPM using a massless link connecting the center of pressure (COP) to the COM. Specifically, the differential equation of the LIPM (or equivalently, the dynamics of the LIPM) is represented as follows:

$$\ddot{x} = \omega^2(x - u) \tag{3}$$

where $x \in \mathbb{R}^2$ is the horizontal position of the COM, u is the position of the COP on the floor, and $\omega = \sqrt{g/z}$ is the natural frequency of the pendulum (where z is the constant height of the COM, and g is the gravity constant). By defining the divergent component of motion (DCM) [25,26] as $\xi = x + \dot{x}/\omega$, the dynamics of the LIPM can also be written as

$$\dot{x} = \omega(\xi - x) \tag{4}$$

$$\dot{\xi} = \omega(\xi - u) \tag{5}$$

In (4) and (5), the dynamics of the LIPM can be divided into (1) the stable parts, where the COM converges to the DCM, and (2) the unstable part, where the DCM is pushed away by the COP. Solving (5) gives the solution

$$\xi_T = (\xi - u)e^{\omega T} + u. \tag{6}$$

This is very convenient for this representation, as we can ensure stable walking by preventing the DCM from diverging without considering the stable part of the system. As discussed in [25,26], by setting the terminal condition (captured state) at the end of a predefined number of steps, we can recursively compute the desired DCM at the end of the current step. Then, by further introducing the DCM offset (the difference between the next step location and the DCM at the end of the step), we can always determine the next step location of the robot.

4.2. Quintic Polynomial Trajectory Planning in Joint Space

After calculating the next step location, we should move the robot to the desired position quickly and accurately. In addition, to avoid vibrations and impacts on the robot’s joints, the acceleration and jerk of the joint motors need to be continuous. To ensure accuracy, stability, and continuity, we propose to perform joint interpolation for the leg at each moment to control its movement. First, the angular velocity and the angle of the joints should be calculated at the time when the robot reaches the final foot location position at the desired velocity. We use the inverse kinematic equation to determine the rotation angle of the joints, and we calculate the angular velocity of the joints as follows:

$$\dot{\Theta} = J^{-1}\dot{X} \tag{7}$$

where Θ is the angle of each joint, J^{-1} is the inverse of the Jacobian matrix of the leg robot, and \dot{X} represents the position and posture of the foot in Cartesian space. Next, we use quintic polynomials to plan the trajectories of the joints. Formally, the quintic polynomials are calculated as follows:

$$\bar{\gamma}_i(t) = c_{i,0} + c_{i,1}t + c_{i,2}t^2 + c_{i,3}t^3 + c_{i,4}t^4 + c_{i,5}t^5 \tag{8}$$

$$\dot{\bar{\gamma}}_i(t) = c_{i,1} + 2c_{i,2}t + 3c_{i,3}t^2 + 4c_{i,4}t^3 + 5c_{i,5}t^4 \tag{9}$$

$$\ddot{\bar{\gamma}}_i(t) = 2c_{i,2} + 6c_{i,3}t + 12c_{i,4}t^2 + 20c_{i,5}t^3 \tag{10}$$

where t is the time when executing the desired trajectory, $\bar{\gamma}_i(t)$ is the polynomial of the joint angle at instant t , $\dot{\bar{\gamma}}_i(t)$ is the polynomial of the joint angular velocity at instant t , and $\ddot{\bar{\gamma}}_i(t)$ is the polynomial of the joint angular acceleration at instant t .

The robot starts from the ready state, and we set the time to $t = 0$. Meanwhile, we set the ready state of the joint angles as θ_{ready} . The initial angular velocity and angular acceleration are both set to 0. When the time is $t = t_s$, the robot arrives at the desired position at the desired velocity. We obtain the joint angle and angular velocity using (7) and set the angular acceleration to 0.

4.3. Joint-Angle Correction System

Given a target angle for the knee joint, the actual motion angle of the knee joint may have errors, which can cause changes in the position of the leg and affect the angles of the hip joint and ankle joint. To ensure smooth movement of the leg, compensation is necessary to eliminate these errors and ensure that all the joints move along the specified trajectories each time they are executed. To this end, we introduce the concept of the “virtual leg”, which is an imaginary leg that connects the hip joint and the ankle joint, as depicted in Figure 5. A new method based on the “virtual leg” is presented, which can control the robot to the desired location in a relatively smooth way.

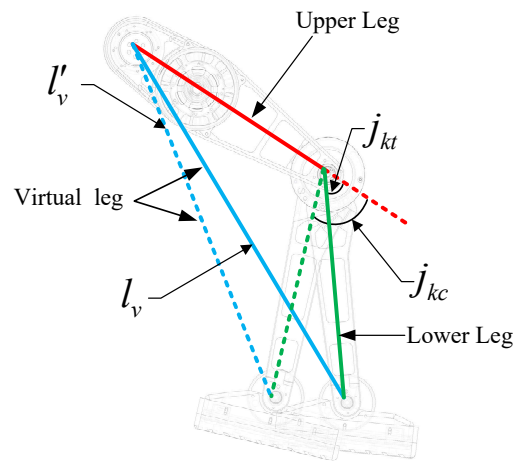


Figure 5. The joint-angle correction system.

As shown in Figure 5, the length of the virtual leg can be expressed as:

$$l_v = 2l \cos(-j_{kt}/2), \tag{11}$$

and

$$l'_v = 2l \cos(-j_{kc}/2) \tag{12}$$

where l is the length of the upper leg and the lower leg, and j_{kt} and j_{kc} are the target knee-joint angle and the current knee-joint angle, respectively. Taking the derivatives of l_v and l'_v , we have

$$\frac{\partial l_v}{\partial t} = \frac{\partial l_v}{\partial j_{kt}} \frac{\partial j_{kt}}{\partial t} = (-l \sin(j_{kt}/2)) \frac{\partial j_{kt}}{\partial t}, \tag{13}$$

and

$$\frac{\partial l'_v}{\partial t} = \frac{\partial l'_v}{\partial j_{kc}} \frac{\partial j_{kc}}{\partial t} = (-l \sin(j_{kc}/2)) \frac{\partial j_{kc}}{\partial t}. \tag{14}$$

Let $W = -l \sin(j_{kt}/2)$ and $W' = -l \sin(j_{kc}/2)$, and then,

$$\dot{l}_v = W \dot{j}_{kt}, \tag{15}$$

and

$$\dot{l}'_v = W' \dot{j}_{kc}. \tag{16}$$

By the law of conservation of energy, we have

$$\tau \dot{j}_{kt} = F \dot{l}_v, \tag{17}$$

where τ is the output torque of the knee joint, and F is the force exerted on the virtual leg. Since $\dot{l}_v = W \dot{j}_{kt}$,

$$\tau \dot{j}_{kt} = F W \dot{j}_{kt} \tag{18}$$

Thus, we have

$$\tau = F W \tag{19}$$

The discrepancies between the target angle and the actual angle of the knee joint give rise to variances in the virtual leg length. By controlling these variances in the virtual leg length,

the robot can reach the desired location in a relatively smooth way. Specifically, the PD controller for the force exerted on the virtual leg is designed as follows

$$F = K_l(l_v - l'_v) - D_l \dot{l}'_v \tag{20}$$

where K_l and D_l are the PD parameters of the force controller. Substituting (20) into (19), we have

$$\tau = W(K_l(l_v - l'_v) - D_l \dot{l}'_v). \tag{21}$$

Then, from (11), (12), and (21), we have

$$\begin{aligned} \tau &= W[K_l(2l \cos(-j_{kt}/2) - 2l \cos(-j_{kc}/2)) - D_l W' \dot{j}_{kc}] \\ &= 2K_l W[-2l \sin(1/2 j_{kt}) \sin(1/4(j_{kt} - j_{kc}))] - D_l W W' \dot{j}_{kc}. \end{aligned}$$

Since $W = -l \sin(j_{kt}/2)$, we have

$$\begin{aligned} \tau &= 2K_l W[2W \sin(1/4(j_{kt} - j_{kc}))] - D_l W W' \dot{j}_{kc} \\ &= K_l W^2 \sin(j_{kt} - j_{kc}) - D_l W W' \dot{j}_{kc}. \end{aligned}$$

Since $j_{kt} - j_{kc}$ is small, $\sin(j_{kt} - j_{kc}) \approx j_{kt} - j_{kc}$. Thus, to stabilize the knee-joint angle to the desired value, the input torque for the knee joint is

$$\begin{aligned} \tau &= K_l W^2(j_{kt} - j_{kc}) - D_l W W' \dot{j}_{kc} \\ &= K_l W^2(\tau_{mk}/K r_{mk} + \frac{1}{3}(m_{kt} - m_{kc})) - D_l W W' \dot{j}_{kc} \end{aligned} \tag{22}$$

Remark 2. In this paper, we adopt the controller shown in (22). As we can see, although K_l and D_l are constant numbers, the values of W and W' change based on the value of the knee-joint angle, which leads to changing PD parameters for the knee-joint controller. This is in contrast to the traditional PD controllers shown in (1) and (2), which have constant PD parameters K_a , D_a , K_k , and D_k , regardless of the changing joint angles. Their performance is tested in the following section.

The structure of the biped robot system is depicted in Figure 6. When the system makes a locomotion state transition from double support to lifting the right/left leg, the next step location of the robot is determined using the linear inverted pendulum model and the DCM algorithm described in Section 4.1. To control the robot to the desired location, a swing leg foot trajectory (the position and posture trajectory of the foot in Cartesian space) is planned. Using the inverse kinematic equation, the joint-angle trajectory can be determined, as described in (7). Then, using (8), (9), and (10), we can obtain the angle, angular velocity, and angular acceleration of the swing leg joints at each instant. Instead of directly applying torques to the joints based on angle error feedback, the joint-angle correction system adjusts the control inputs according to the variance of the visual leg position. The above process is repeated after each locomotion state transition.

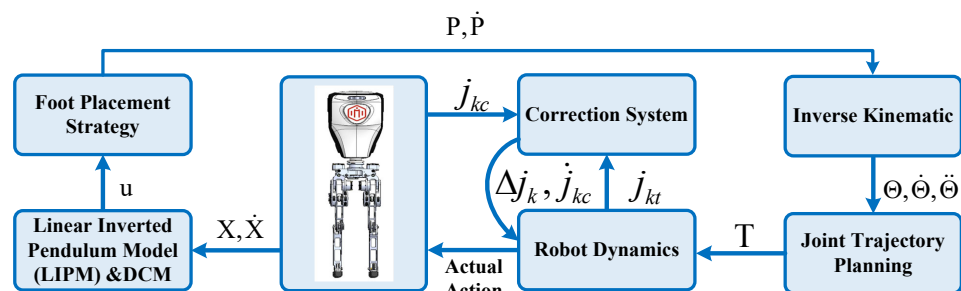


Figure 6. The structure of the biped robot system.

5. Experiments

In this section, we evaluate the theoretical results through experiments. The experimental program runs on the embedded processor (Rockchip RK3399 SoC) of the M03 biped robot. The robot has a height of 120 cm and a total weight of 15.6 kg. In the real robot experiment, the mass of the robot is adjustable (by tying a blue block with a mass of 3.0 kg), as shown in Figure 7. Joint states and joint commands are sent to the robot via Ethernet using TCP/IP. The control commands and status information are updated at a frequency of 200 Hz.

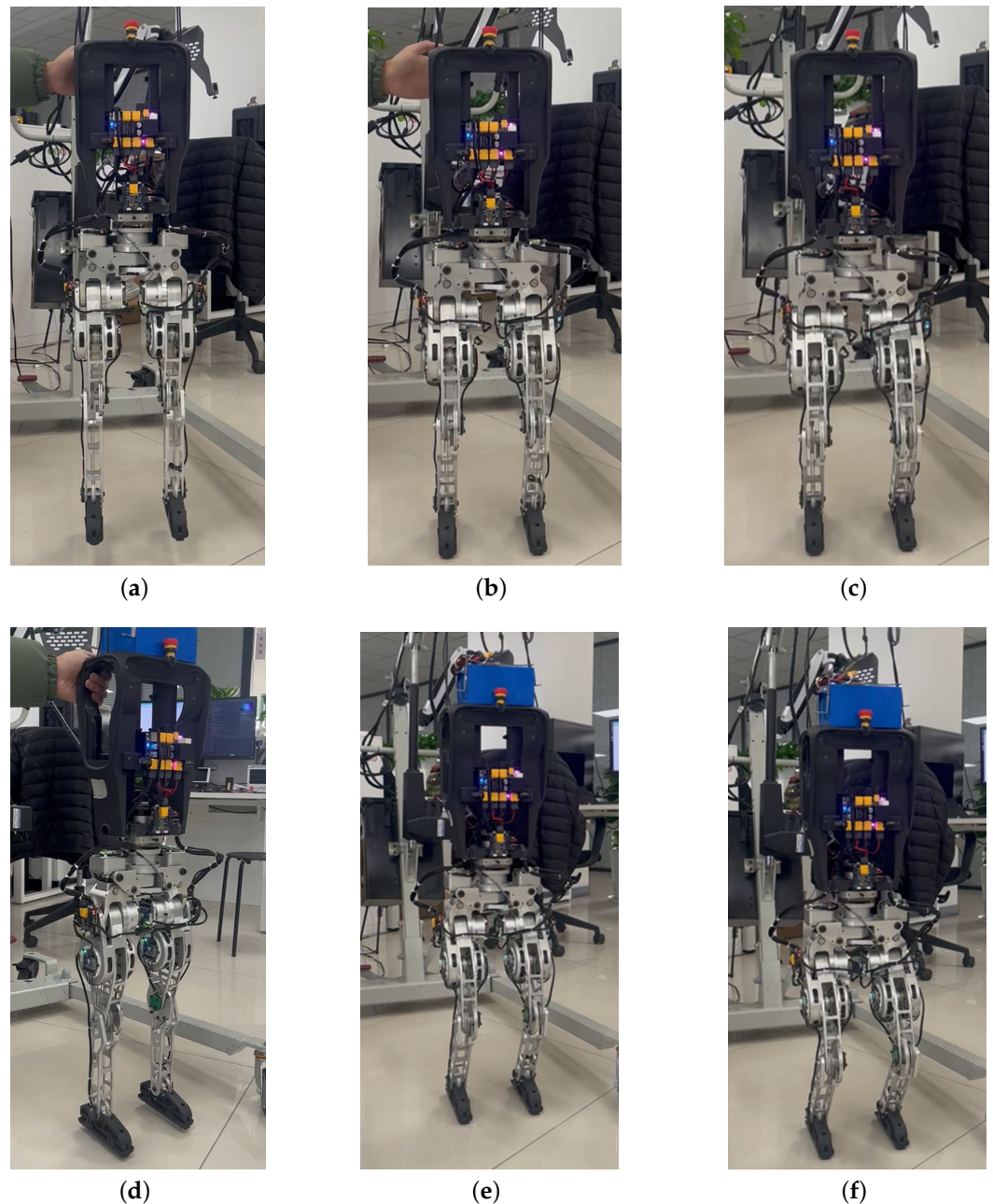


Figure 7. Squat-stand motions with and without an extra load. (a) Phase 1 for squat-stand motions without an extra load. (b) Phase 2 for squat-stand motions without an extra load. (c) Phase 3 for squat-stand motions without an extra load. (d) Phase 1 for squat-stand motions with an extra load. (e) Phase 2 for squat-stand motions with an extra load. (f) Phase 3 for squat-stand motions with an extra load.

As shown in Figure 7, we first evaluated the error estimation algorithm proposed in Section 3 by performing squat-stand motions with and without an extra load. The knee-joint position controller was enabled when measuring the motor-joint errors. The experiments were conducted on the robot using different parameters for the knee-joint position PD controller, with and without the joint-angle correction system, and with and without an extra load. Specifically, when there was no joint-angle correction system, the controller (with constant PD parameters) exerted torque to the corresponding motor based only on the difference between the target angle and the current angle of the knee joint without considering the variance of the virtual leg length. The details are given in (1) and (2). However, when there was a joint-angle correction system, the controller further considered the variance of the virtual leg length when stabilizing the knee-joint angle to its target value. In addition, we tested our error estimation algorithm by varying the values of K_k and D_k in (2) and K_l and D_l in (22).

For brevity, the considered conditions were divided into four cases: in the first case (Case 1), there was no joint-angle correction system, and the PD parameters in (2) were $K_k = 2$ and $D_k = 2$; in the second case (Case 2), there was no joint-angle correction system, and the PD parameters in (2) were $K_k = 1$ and $D_k = 1$; in the third case (Case 3), there was a joint-angle correction system, and the PD parameters in (22) were $K_l = 2$ and $D_l = 2$; and in the fourth case (Case 4), there was a joint-angle correction system, and the PD parameters in (22) were $K_l = 1$ and $D_l = 1$.

In our first experiment, we determined the knee-joint errors caused by elastic deformation (ek1) and motor execution (ek2) when performing squat-stand motions, as shown in Figure 8. As we can see in Figure 8a,d; Figure 8b,c; Figure 8e,h; and Figure 8f,g, the knee-joint errors were reduced due to the joint-angle correction system. This indicates that the proposed smooth control approach effectively suppressed the joint errors caused by elastic deformation and motor execution. Meanwhile, as we can see in Figure 8a,e; Figure 8b,f; Figure 8c,g; and Figure 8d,h, the extra load had a relatively small effect on the knee-joint errors.

In our second experiment, we examined whether the knee-joint angle errors estimated using the proposed methods were consistent with the real knee-joint angle errors. The experimental results for the robot both with and without an extra load are shown in Figure 9. In Figure 9, the red solid line (ek1*) represents the estimated knee-joint angle errors, and the blue dashed line (ek1) represents the real knee-joint angle errors, which were measured using the absolute encoder mounted at the knee joint. The vertical axes represent the knee-joint angles. As shown in Figure 9, the proposed error estimation methods performed better with small PD parameters compared to large PD parameters. This was mainly attributed to the proposed smooth control approach, which resulted in less tension on the steel wire rope. For controllers with large PD parameters, a more robust error estimation method is needed, which will be discussed in our future work. In general, the tests validated the effectiveness of the knee-joint error estimation methods given in Section 3.

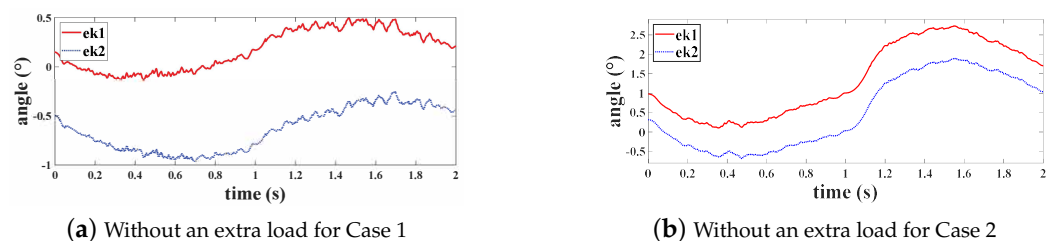


Figure 8. Cont.

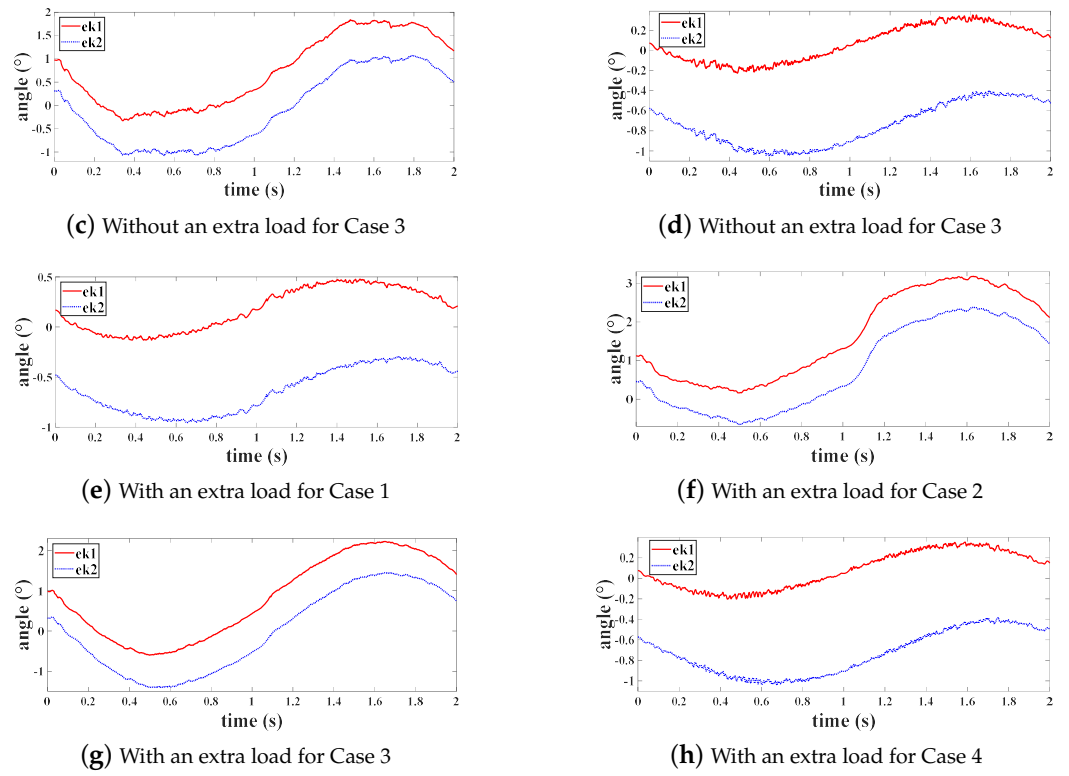


Figure 8. Knee-joint errors when performing squat-stand motions.

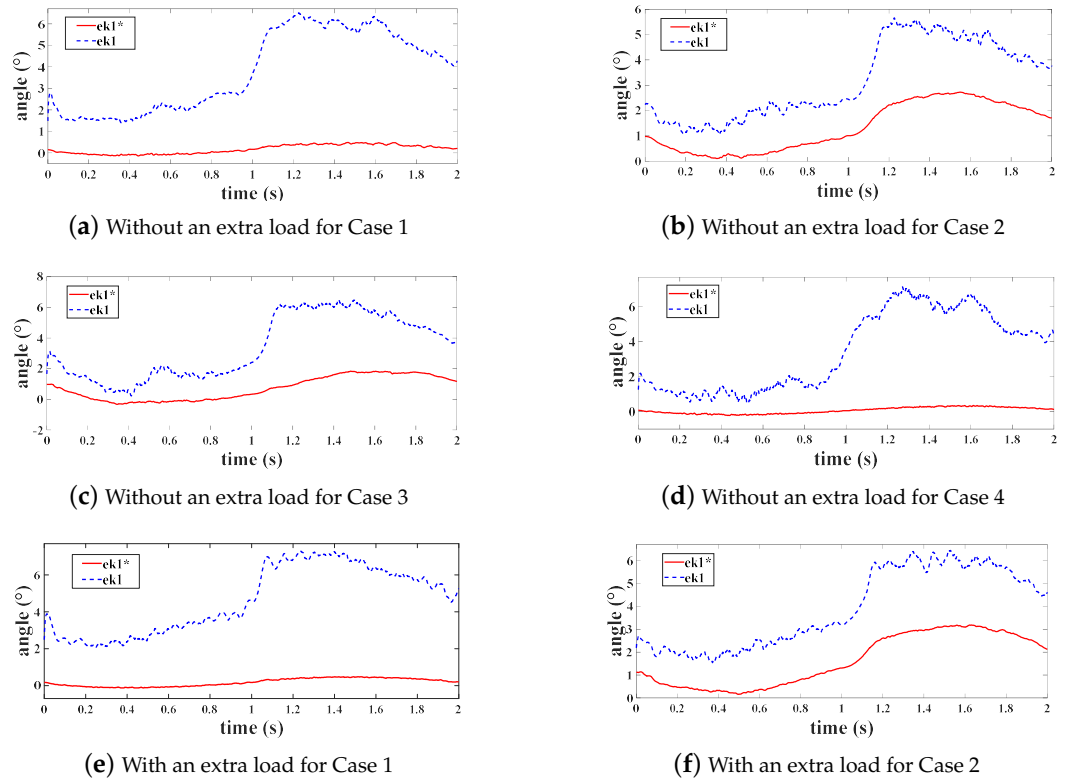


Figure 9. Cont.

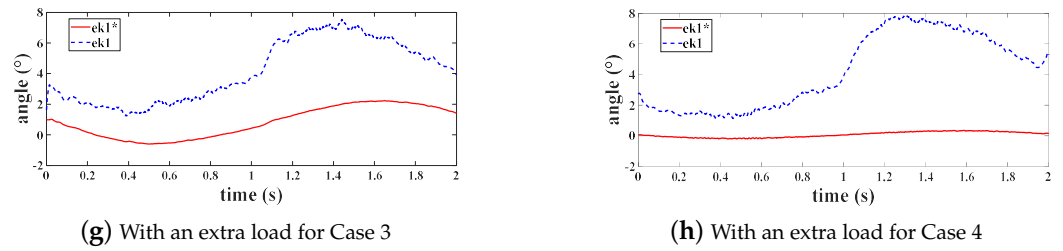


Figure 9. Comparison between the estimated joint-angle errors and the real joint-angle errors.

In the third experiment, with the given target knee-joint angles (jkt), we tested the effects of the error estimation methods on reducing joint-angle errors. The joint-angle control methods introduced in the aforementioned experiments were used in this test. In Figures 10 and 11, the vertical axes represent the knee-joint angles. Despite significant differences between the control methods, PID parameters, and body mass, Figures 10 and 11 show that during the experiments, the knee-joint angles always converged to their target values. These results show that the knee-joint angles (jk) obtained during the experiments and the desired knee-joint angles were virtually consistent.

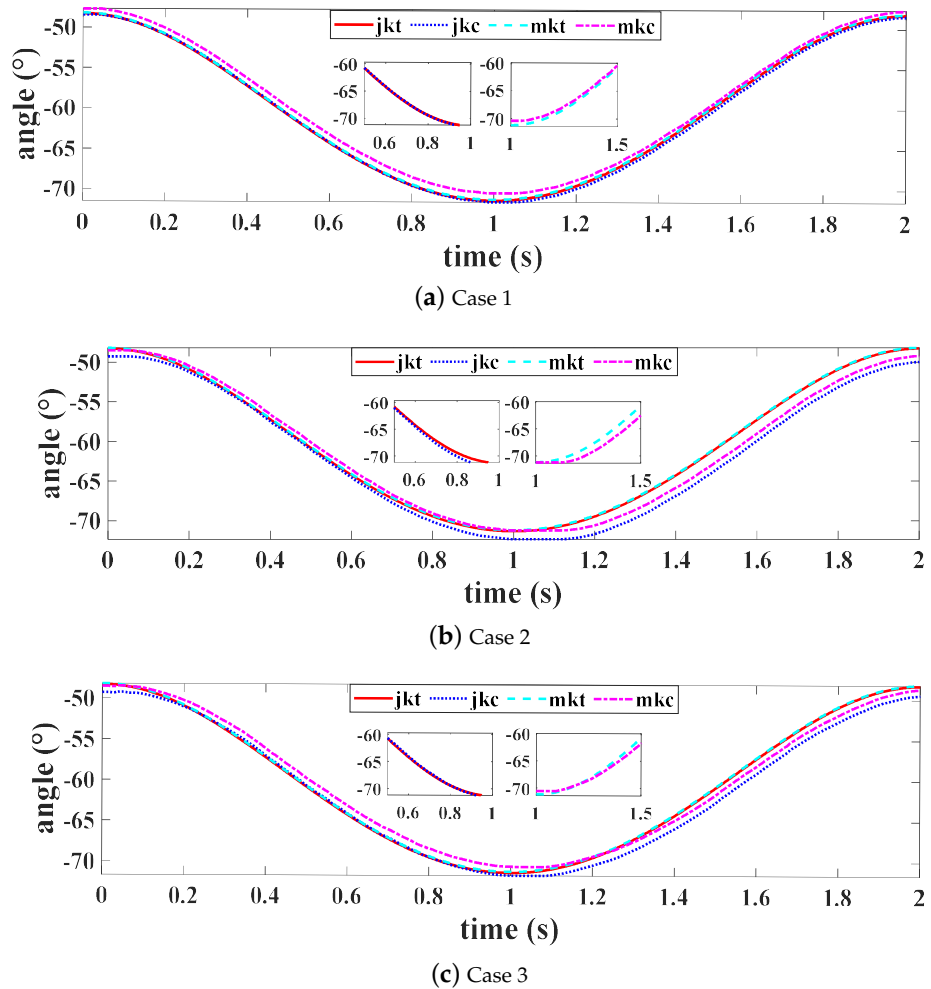


Figure 10. Cont.

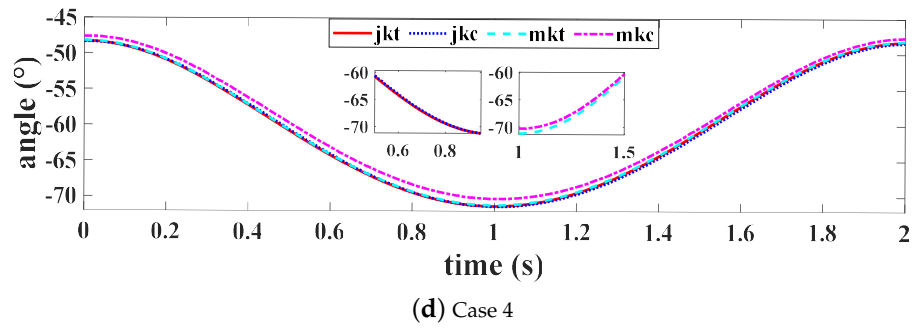


Figure 10. The knee-joint positions for the different cases without an extra load.

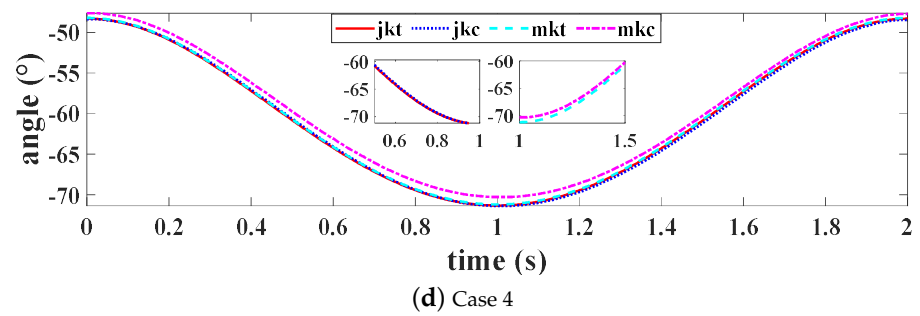
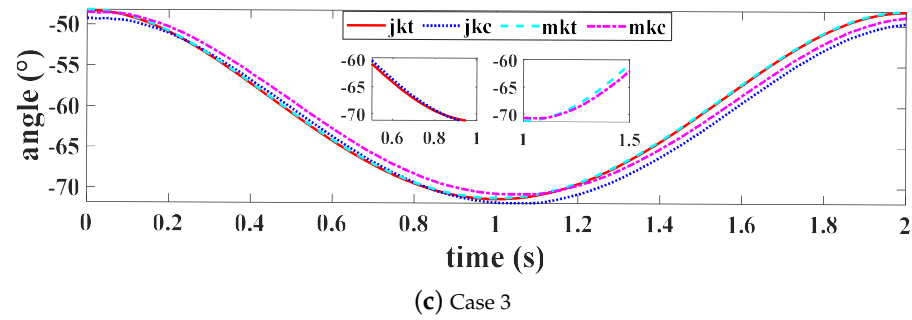
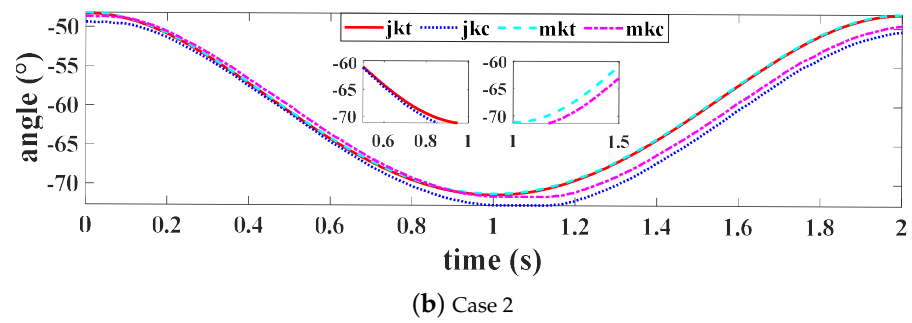
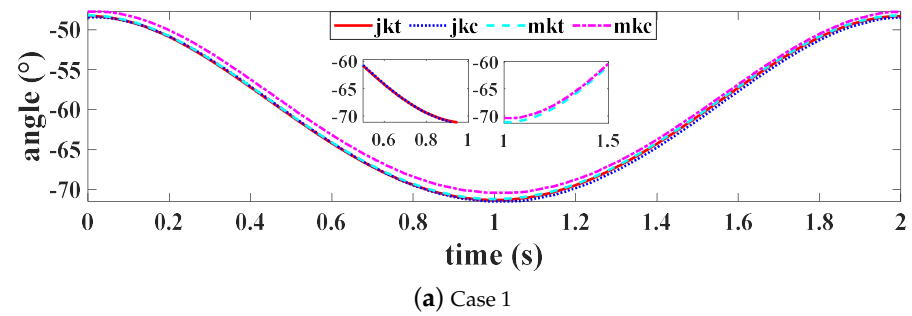
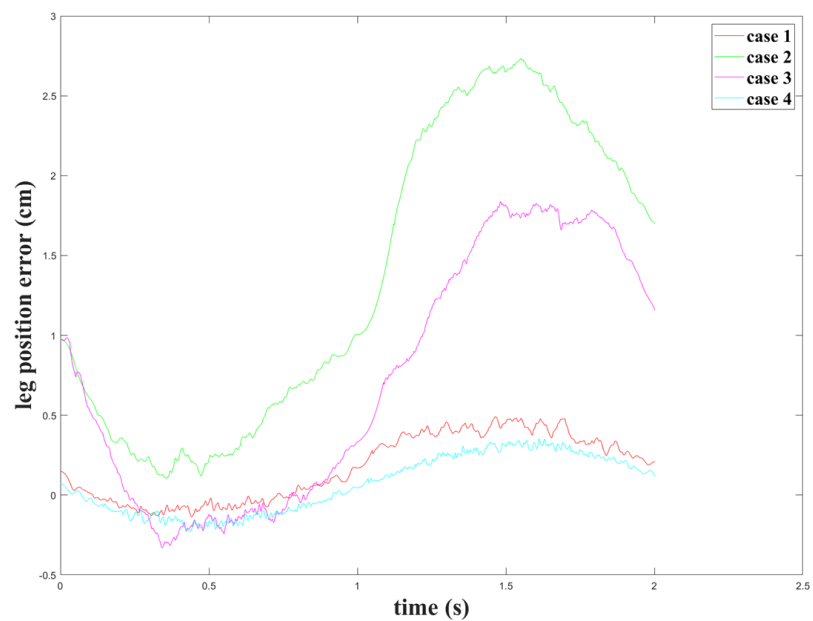
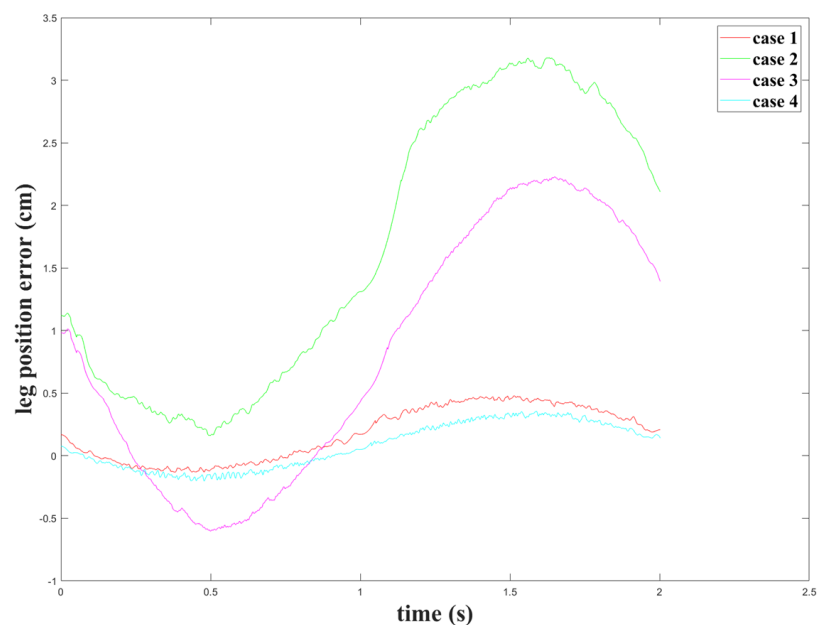


Figure 11. The knee-joint positions for the different cases with an extra load.

In the fourth experiment, we tested the performance of the proposed control approach through a back-and-forth walking task. The experimental results are shown in Figures 12 and 13. Figure 12 shows the leg position errors (the position difference between the virtual leg and the leg) for the different cases during the motions. We can see that the errors were constrained within a relatively small range and did not diverge toward infinitely large values. In Figure 13a, the blue line represents the desired velocities of the COM at the end of each step, and the red line represents the real velocities of the COM at each instant. Figure 13a indicates that the robot always attained the desired velocity at the end of each step. Figure 13b shows the target and current positions of the legs during walking. As shown in Figure 13b, the desired positions for the swinging leg and the stance leg were reached. These results justify the robustness of the control approach.

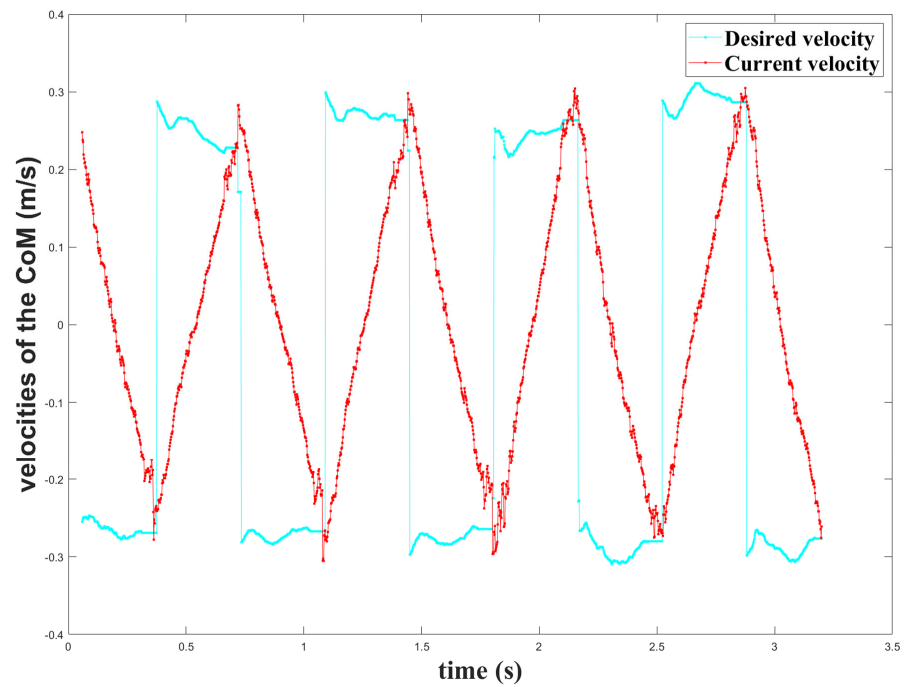


(a) Without an extra load

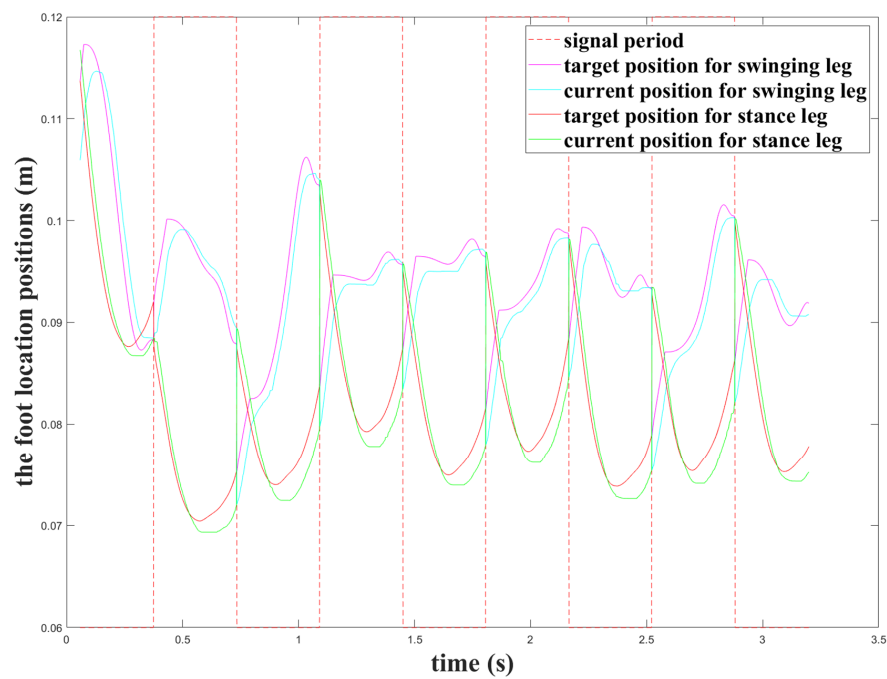


(b) With an extra load

Figure 12. Position errors between the virtual leg and the leg.



(a) Velocities of the CoM



(b) Positions of the swinging and stance legs

Figure 13. Performance of the proposed control approach.

The accompanying videos show two successful experiments conducted with our robot. In the first video, the robot was required to perform a squat-stand motion by controlling the knee joints. In the second video, the robot was given a reference velocity to perform a forward motion. Specifically, the velocities were set at $v_x = 0.15$ m/s, followed by $v_y = 0.05$ m/s.

6. Conclusions

In this paper, we have proposed a low-inertia and high-stiffness cable-driven biped robot. Using the developed model, we have proposed an optimal control mechanism to

guide the robot to the desired location at the desired velocity. This is accomplished in two steps: the first step involves estimating the motor errors caused by the elastic deformation of the steel wire rope, and the second step involves enforcing precise motor control by considering both the motor errors and the variance of the visual leg position.

The algorithm is sufficiently efficient to account for joint position errors in real time. The effectiveness of both the developed model and algorithm is demonstrated through simulation results.

A potential future research direction is to estimate the elastic deformation of the steel wire rope in a more efficient way. Further, other optimality notions tailored to real-world applications could be defined, and a new set of algorithms could be developed to achieve these notions.

Author Contributions: Conceptualization, J.T. and Y.H.; methodology, J.T., H.M. and Y.Z.; software, Y.Z.; validation, Y.H., J.Z. and J.L.; formal analysis, J.T., Y.H. and Y.Z.; investigation, J.Z.; resources, J.L. and J.Z.; data curation, Y.Z.; writing—original draft preparation, J.T. and Y.H.; writing—review and editing, J.T., Y.H. and Y.Z.; visualization, J.T. and Y.H.; supervision, J.L. and J.Z.; project administration, J.L. and J.Z.; funding acquisition, J.L. and J.Z. All authors have read and agreed to the published version of the manuscript.

Funding: This research was funded by the National Natural Science Foundation of China under grant 92048205 and the Pujiang Talents Plan of Shanghai under grant 2019PJD035.

Data Availability Statement: Data are contained within the article.

Conflicts of Interest: The authors declare no conflicts of interest.

References

- Hinojosa, E.H.; Bhounsule, P.A. Data-driven Identification of a Non-homogeneous Inverted Pendulum Model for Enhanced Humanoid Control. In Proceedings of the 2023 IEEE-RAS 22nd International Conference on Humanoid Robots (Humanoids), Austin, TX, USA, 12–14 December 2023; pp. 1–8.
- Kashyap, A.; Parhi, D. Dynamic Walking of Humanoid Robot on Flat Surface Using Amplified LIPM Plus Flywheel Model. *Int. J. Intell. Unmanned Syst.* **2022**, *10*, 316–329. [[CrossRef](#)]
- Park, H.Y.; Kim, J.H.; Yamamoto, K. A New Stability Framework for Trajectory Tracking Control of Biped Walking Robots. *IEEE Trans. Ind. Inform.* **2022**, *18*, 6767–6777. [[CrossRef](#)]
- Imanishi, K.; Sugihara, T. Autonomous Biped Stepping Control Based on the LIPM Potential. In Proceedings of the 2018 IEEE-RAS 18th International Conference on Humanoid Robots (Humanoids), Beijing, China, 6–9 November 2018; pp. 280–283.
- Urbann, O.; Schwarz, I.; Hofmann, M. Flexible Linear Inverted Pendulum Model for cost-effective biped robots. In Proceedings of the 2015 IEEE-RAS 15th International Conference on Humanoid Robots (Humanoids), Seoul, Republic of Korea, 3–5 November 2015; pp. 128–131.
- Ahn, J.; Lee, J.; Sentis, L. Data-Efficient and Safe Learning for Humanoid Locomotion Aided by a Dynamic Balancing Model. *IEEE Robot. Autom. Lett.* **2020**, *5*, 4376–4383. [[CrossRef](#)]
- Duan, H.; Malik, A.; Dao, J.; Saxena, A.; Green, K.; Siekmann, J.; Fern, A.; Hurst, J. Sim-to-Real Learning of Footstep-Constrained Bipedal Dynamic Walking. In Proceedings of the 2022 International Conference on Robotics and Automation (ICRA), Philadelphia, PA, USA, 23–27 May 2022; pp. 10428–10434.
- Koryakovskiy, I.; Kudruss, M.; Vallery, H.; Babuška, R.; Caarls, W. Model-Plant Mismatch Compensation Using Reinforcement Learning. *IEEE Robot. Autom. Lett.* **2018**, *3*, 2471–2477. [[CrossRef](#)]
- Ding, J.; Han, L.; Ge, L.; Liu, Y.; Pang, J. Robust Locomotion Exploiting Multiple Balance Strategies: An Observer-Based Cascaded Model Predictive Control Approach. *IEEE/ASME Trans. Mechatron.* **2022**, *27*, 2089–2097. [[CrossRef](#)]
- Hamed, K.A.; Kim, J.; Pandala, A. Quadrupedal Locomotion via Event-Based Predictive Control and QP-Based Virtual Constraints. *IEEE Robot. Autom. Lett.* **2020**, *5*, 4463–4470. [[CrossRef](#)]
- Shafiee-Ashtiani, M.; Yousefi-Koma, A.; Shariat-Panahi, M. Robust Bipedal Locomotion Control Based on Model Predictive Control and Divergent Component of Motion. In Proceedings of the 2017 IEEE International Conference on Robotics and Automation (ICRA), Shanghai, China, 29–31 December 2017; pp. 3505–3510.
- Khadij, M.; Herzog, A.; Moosavian, S.A.A.; Righetti, L. Walking Control Based on Step Timing Adaptation. *IEEE Trans. Robot.* **2020**, *36*, 629–643. [[CrossRef](#)]
- Bailly, F.; Carpentier, J.; Benallegue, M.; Watier, B.; Soueres, P. Estimating the Center of Mass and the Angular Momentum Derivative for Legged Locomotion—A Recursive Approach. *IEEE Robot. Autom. Lett.* **2019**, *4*, 4155–4162. [[CrossRef](#)]

14. Ameri, A.; Molaei, A.; Khosravi, M.A.; Aghdamp, A.G.; Dargahi, J. Modeling and Control of Cable-Driven Parallel Robots with Non-affine Dynamics. In Proceedings of the 2021 60th IEEE Conference on Decision and Control (CDC), Austin, TX, USA, 13–17 December 2021; pp. 5582–5587.
15. Zou, Y.; Hu, Y.; Cao, H.; Xu, Y.; Yu, Y.; Lu, W.; Xiong, H. Data-Driven Kinematic Control Scheme for Cable-Driven Parallel Robots Allowing Collisions. In Proceedings of the 2022 IEEE/RSJ International Conference on Intelligent Robots and Systems (IROS), Kyoto, Japan, 23–27 October 2022; pp. 5003–5008.
16. Roozing, W.; Ren, Z.; Tsagarakis, N. An Efficient Leg with Series–Parallel and Biarticular Compliant Actuation: Design Optimization, Modeling, and Control of the ELeg. *Int. J. Robot. Res.* **2021**, *40*, 37–54. [[CrossRef](#)]
17. Kim, M.C.; Choi, H.; Piao, J.; Kim, E.s.; Park, J.O.; Kim, C.S. Remotely Manipulated Peg-in-Hole Task Conducted by Cable-Driven Parallel Robots. *IEEE/ASME Trans. Mechatron.* **2022**, *27*, 3953–3963. [[CrossRef](#)]
18. Ida, E.; Bruckmann, T.; Carricato, M. Rest-to-Rest Trajectory Planning for Underactuated Cable-Driven Parallel Robots. *IEEE Trans. Robot.* **2019**, *35*, 1338–1351. [[CrossRef](#)]
19. Liu, Z.; Zhang, X.; Cai, Z.; Peng, H.; Wu, Z. Real-Time Dynamics of Cable-Driven Continuum Robots Considering the Cable Constraint and Friction Effect. *IEEE Robot. Autom. Lett.* **2021**, *6*, 6235–6242. [[CrossRef](#)]
20. Zhang, J.; Shen, J.; Liu, Y.; Hong, D. Design of a Jumping Control Framework with Heuristic Landing for Bipedal Robots. In Proceedings of the 2023 IEEE/RSJ International Conference on Intelligent Robots and Systems (IROS), Detroit, MI, USA, 1–5 October 2023; pp. 8502–8509.
21. Bryson, J.; Agrawal, S. Analysis of Optimal Cable Configurations in the Design of a 3-DOF Cable-Driven Robot Leg. In Proceedings of the ASME 2014 International Design Engineering Technical Conferences and Computers and Information in Engineering Conference, Buffalo, NY, USA, 17–20 August 2014.
22. Ficanha, E.; Rastgaar, M.; Kaufman, K. A Two-axis Cable-Driven Ankle-Foot Mechanism. *Robot. Biomim.* **2014**, *1*, 17. [[CrossRef](#)]
23. Hidayah, R.; Bishop, L.; Jin, X.; Chamarthy, S.; Stein, J.; Agrawal, S.K. Gait Adaptation Using a Cable-Driven Active Leg Exoskeleton (C-ALEX) with Post-Stroke Participants. *IEEE Trans. Neural Syst. Rehabil. Eng.* **2020**, *28*, 1984–1993. [[CrossRef](#)] [[PubMed](#)]
24. Demirel, M.; Kiper, G.; Carbone, G.; Ceccarelli, M. Design of a Novel Hybrid Cable-Constrained Parallel Leg Mechanism for Biped Walking Machines. *Robot. Int. J. Inf. Educ. Res. Robot. Artif. Intell.* **2023**, *41*, 1778–1793. [[CrossRef](#)]
25. Takenaka, T.; Matsumoto, T.; Yoshiike, T. Real Time Motion Generation and Control for Biped Robot—1st Report: Walking Gait Pattern Generation. In Proceedings of the 2009 IEEE/RSJ International Conference on Intelligent Robots and Systems, St. Louis, MI, USA, 11–15 October 2009; pp. 1084–1091.
26. Englsberger, J.; Ott, C.; Albu-Schäffer, A. Three-Dimensional Bipedal Walking Control Based on Divergent Component of Motion. *IEEE Trans. Robot.* **2015**, *31*, 355–368. [[CrossRef](#)]

Disclaimer/Publisher’s Note: The statements, opinions and data contained in all publications are solely those of the individual author(s) and contributor(s) and not of MDPI and/or the editor(s). MDPI and/or the editor(s) disclaim responsibility for any injury to people or property resulting from any ideas, methods, instructions or products referred to in the content.